Editors' Suggestion

Dimensionality-Dependent Exciton Dispersion in a Single-Band Mott Insulator

Zhibin Su,[1,2] Junjian Mi,[3,4] Shaohua Yan,[5,6] Jiade Li,[1,7] Siwei Xue,[1,8] Zhiyu Tao,[1,2] Enling Wang,[1,2] Xiongfei Shi,[1,2] Hechang Lei,[5,6,*] Zhuan Xu,[3,4,9,†] Jiandong Guo,[1,2,‡] and Xuetao Zhu[1,2,§]

[1]*Beijing National Laboratory for Condensed Matter Physics and Institute of Physics, Chinese Academy of Sciences, Beijing 100190, China*
[2]*School of Physical Sciences, University of Chinese Academy of Sciences, Beijing 100049, China*
[3]*School of Physics, Zhejiang University, Hangzhou 310058, China*
[4]*State Key Laboratory of Silicon and Advanced Semiconductor Materials, Zhejiang University, Hangzhou 310027, China*
[5]*School of Physics and Beijing Key Laboratory of Opto-electronic Functional Materials and Micro-nano Devices, Renmin University of China, Beijing 100872, China*
[6]*Key Laboratory of Quantum State Construction and Manipulation (Ministry of Education), Renmin University of China, Beijing 100872, China*
[7]*International Center for Quantum Materials, and Electron Microscopy Laboratory, School of Physics, Peking University, Beijing 100871, China*
[8]*Department of Physics, Fuzhou University, Fuzhou 350108, Fujian, China*
[9]*Hefei National Laboratory, Hefei 230088, China*

Excitonic band structure is critical for investigating exciton dynamics. Theoretically, quantum effects from exchange scattering between electron-hole pairs significantly modulate exciton dispersion. Here, we report the direct observation of dimensionality-dependent exciton dispersion in a single-band Mott insulator Nb_3Cl_8 through high-resolution electron energy loss spectroscopy. In the high-temperature phase, the exciton in Nb_3Cl_8 hosts an exceptionally large binding energy, and exhibits clear quasi-two-dimensional massless linear dispersion. In contrast, in the low-temperature phase, the exciton splits into two bands, both displaying three-dimensional parabolic dispersion. These dramatic changes in the exciton dispersion stem from the dimensional mutation driven by a substantial enhancement of interlayer coupling across the phase transition. This Letter provides a clear and typical example of how exciton behavior evolves with dimensionality.

Excitons, which are electron-hole pairs bound by Coulomb interaction, play a crucial role in the optoelectronic properties of semiconductors [1–3]. Conventionally, research on excitonic properties has primarily focused on bright excitons, which can be directly excited by light [2,4]. In recent years, there has been growing interest in dark excitons [4–8], especially the momentum-forbidden dark excitons [5,9,10], which greatly influence the exciton dynamics. The bright excitons and the momentum-forbidden dark excitons can be considered as distinct parts of excitonic band structures. The excitonic band structure has significant impacts on the performance of semiconductors, influencing key properties such as radiative lifetime [11–14], quantum yield [13,15], and exciton diffusion coefficient [16–18]. Therefore, understanding the excitonic energy band structure is essential for gaining deep insights into exciton dynamics.

Microscopically, due to the quantum effects arising from exchange scattering between electron-hole pairs, the dispersion of an excitonic energy band is strongly modulated by the dimensionality of the system. Macroscopically, this dependence arises because the dimensionality influences the Coulomb screening strength through the system's dielectric environment. In three-dimensional (3D) semiconductors [Fig. 1(a)], the strong Coulomb screening inherent to the 3D space results in Wannier excitons displaying a parabolic dispersion [Fig. 1(b)] [3,16]. In contrast, when the system's dimensionality is reduced to two-dimensional (2D) [Fig. 1(c)], the Coulomb screening is confined to the 2D plane, and thus the excitons exhibit distinctive massless linear dispersions near the Brillouin zone (BZ) center [Fig. 1(d)]—a phenomenon predicted in archetypical 2D materials such as h-BN, monolayer MoS2, and black phosphorus [16,18–21]. In the 2D limit, the loss of massive character not only suppresses the excitonic density of states at the BZ center but also endows the excitons with high, constant group and phase velocities.

*Contact author: hlei@ruc.edu.cn
†Contact author: zhuan@zju.edu.cn
‡Contact author: jdguo@iphy.ac.cn
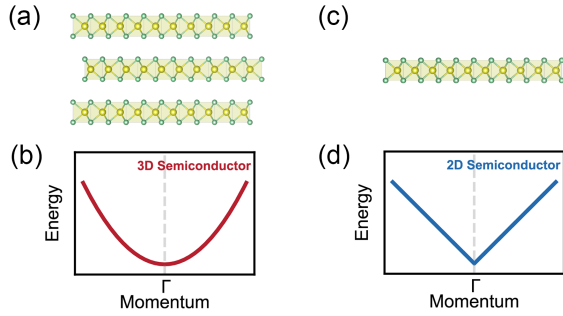§Contact author: xtzhu@iphy.ac.cn

FIG. 1. Illustration of the dimensional effects of excitonic band dispersions. Schematic diagrams of (a) the crystal structures and (b) the corresponding excitonic band structure near the BZ center for typical 3D semiconductors. (c) Crystal structures and (d) the corresponding excitonic band structure for typical 2D semiconductors.
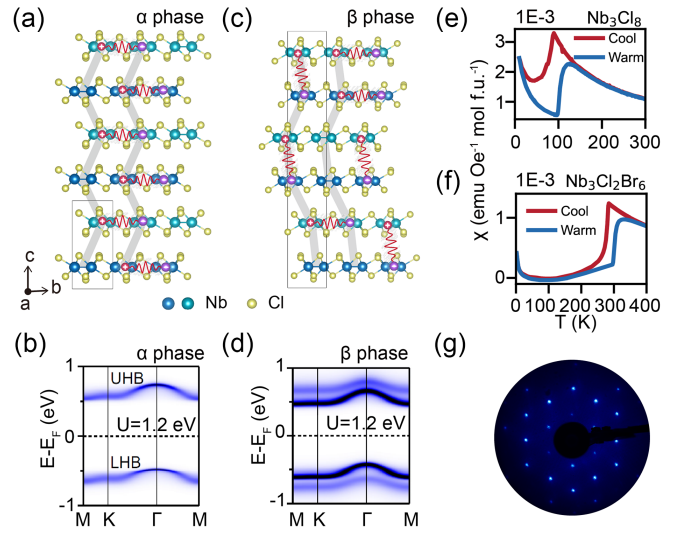

FIG. 2. Structural and electronic properties of Nb_3Cl_8. (a) Side view of the crystal structure and exciton distribution, and (b) the corresponding electronic energy band in the high-temperature phase (α phase) of Nb_3Cl_8. (c) Crystal structure and exciton distribution, and (d) the corresponding electronic energy band in the low-temperature phase (β phase). (e),(f) Magnetic susceptibility as a function of temperature for Nb_3Cl_8 and $Nb_3Cl_2Br_6$. (g) LEED pattern on the (001) surface of Nb_3Cl_8, obtained at room temperature with incident beam energy of 100 eV. Notice that the electronic band structure in (b) and (d) are reproduced from Ref. [35]. Copyright 2025 by the American Physical Society.

Consequently, these unique features enable 2D massless excitons to exhibit shorter radiative lifetimes [12,16], enhanced diffusion rates [16,17], weaker exciton-phonon scattering [17], and the potential for unconventional exciton superfluity [22].

Recently, van der Waals (vdW) materials have emerged as a pivotal platform for investigating excitonic dimensional effects and many-body interactions, owing to their reduced dielectric screening and interlayer connections through weak vdW forces [4,23,24]. Using prototypical vdW materials, experiments have confirmed the parabolic dispersions of Wannier excitons in bulk systems [25–27]. Meanwhile, twisted light has been used to indirectly verify the existence of massless exciton dispersion in monolayer MoS_2 [28]. However, investigations of monolayer WSe_2 using momentum-resolved electron energy loss spectroscopy in a transmission electron microscope (TEM-EELS) have reported a parabolic dispersion [29], which conflicts with theoretical predictions. This apparent discrepancy can be attributed to two concurrent factors: the limited momentum and energy resolution of the technique [30], and the confinement of the linear dispersion to an extremely small momentum region around the BZ center. Together, these limitations prevented the experimental resolution of the linear dispersion feature. Consequently, direct and robust experimental verification of massless exciton dispersion in 2D materials remains lacking, let alone the observation of dimensional effects on exciton dispersion within the same material, which presents an even greater challenge.

Here, we employ High-Resolution Electron Energy Loss Spectroscopy (HREELS) with 2D momentum-energy mapping capabilities [31] to investigate exciton dispersions across the phase transition in Nb_3Cl_8—a textbook single-band Mott insulator recently proposed theoretically [32–34] and validated experimentally [35]. Across the phase transition, we clearly observed the splitting of excitons. Notably, the exciton in the high-temperature phase (α phase) exhibits unambiguous quasi-2D massless dispersion, while in the

low-temperature phase (β phase), the excitons display 3D parabolic dispersion. This drastic change in exciton dispersion arises from the change in system dimensionality, induced by variations in interlayer coupling strength across the phase transition.

Background of Nb_3Cl_8—At room temperature, Nb_3Cl_8 is in its α phase, where each unit cell consists of two monolayers stacked along the c axis via vdW forces [Fig. 2(a)] [36,37]. Within each monolayer, Nb ions spontaneously form Nb_3 trimers, resulting in a breathing kagome lattice [36–38], while weak pd hybridization causes electrons to become strongly localized within the trimers [35]. Concurrently, strong electron correlation leads to the opening of a Mott gap, which in turn provides the pathway for exciton formation, as an intergap transition can also generate an electron-hole pair across the Mott gap. The Nb_3 trimers in adjacent layers are staggered, giving rise to negligible interlayer coupling. These features enable the electronic properties to be effectively described by a monolayer [35,39], with excitons primarily confined to the single layer [Fig. 2(a)]. Thus, in the α phase, Nb_3Cl_8 serves as an ideal quasi-2D single-band Mott insulator, with the valence and conduction bands arising from the lower Hubbard band (LHB) and upper Hubbard band (UHB), both driven by Nb d orbitals [Fig. 2(b)].

As the temperature decreases, Nb_3Cl_8 undergoes a structural phase transition near 100 K [Fig. 2(e)], transforming

from the paramagnetic α phase to the nonmagnetic β phase [36,37,40]. Although the exact structure of the β phase remains under debate, it is clear that interlayer sliding is a key factor. Interlayer sliding aligns the Nb_3 trimers in adjacent layers directly above one another within each bilayer, significantly enhancing the interlayer coupling [Fig. 2(c)]. Therefore, the electronic properties of the β phase are best described as quasi-3D bilayer Nb_3Cl_8, with the significantly enhanced interlayer coupling causing bonding-antibonding splitting in the LHB and UHB [Fig. 2(d)] [32,35]. In this case, the excitons are chiefly located between the two layers [Fig. 2(c)]. Thus, with its uniquely tunable crystal structure, Nb_3Cl_8 serves as a superior model system over conventional semiconductors for probing exciton dimensional effects.

HREELS measurements—As Nb_3Cl_8 is a semiconductor with high electrical resistance as the temperature decreases, significant charging effects occur when performing the HREELS measurements below 250 K, which hinder the observations of the β phase. To diminish the issue of sample charging, we employed the $Nb_3Cl_2Br_6$ sample. The substitution of Br with Cl elevates the phase transition temperature to near room temperature [Fig. 2(f)]. Simultaneously, this substitution narrows the band gap, which in turn effectively suppresses the charging effect [41]. The measured HREELS results of the α phase in $Nb_3Cl_2Br_6$ show features identical to those in Nb_3Cl_8, with only minor energy shifts due to doping [details described in Supplemental Material (SM) [41]]. Here in the main text, we present the α phase data from Nb_3Cl_8 samples, while the β phase data from $Nb_3Cl_2Br_6$ samples. Nb_3Cl_8 and $Nb_3Cl_2Br_6$ single crystals were cleaved *in situ* under ultra-high vacuum, and their surfaces were characterized by low energy electron diffraction (LEED), which shows sharp bright patterns indicating good surface quality [Fig. 2(g)]. All the HREELS measurements were performed with an incident electron energy of 110 eV and an incident angle of 60°.

Exciton splitting—Along the $\bar{\Gamma}\bar{K}$ direction, the 2D energy-momentum mapping of HREELS for the α phase [Fig. 3(a)] and the β phase [Fig. 3(b)] reveals several significant loss signals below 1.5 eV. In the α phase, two well-defined loss peaks are presented, while in the β phase, the shape and intensity of these loss signals change dramatically. To better illustrate these features, we extract the momentum-dependent energy distribution curves (EDCs) for both the α phase [Fig. 3(c)] and the β phase [Fig. 3(d)], fitting the EDCs at the $\bar{\Gamma}$ point. Below 1.5 eV, the fitting results for the α phase show two peaks: a 1.14 eV peak corresponding to interband transitions (IT), and a 0.77 eV peak attributed to the excitation of an exciton (EX), with the identification detailed in SM [41]. These results indicate an optical band gap $E_O = 0.77$ eV and an electronic band gap $E_G = 1.14$ eV, corresponding to excitations from the LHB to the excitonic band and to the UHB, respectively [Fig. 3(e)]. Then, the exciton in the α phase
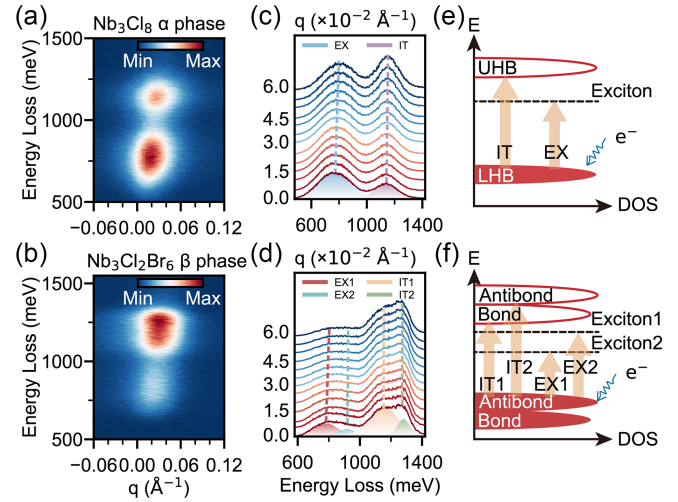

FIG. 3. Exciton splitting from the HREELS measurements. (a),(b) Representative 2D momentum-energy mappings of HREELS along the $\bar{\Gamma}\bar{K}$ direction for Nb_3Cl_8 at 300 K (α phase) and $Nb_3Cl_2Br_6$ at 106 K (β phase). (c),(d) Stacks of momentum-dependent EDCs along $\bar{\Gamma}\bar{K}$ direction, with fitting results for the α phase and β phase. The corresponding momentum values are indicated on the left. For clarity, the EDCs were multiplied by a scaling factor and shifted vertically. (e),(f) Schematic representation of the density of state and corresponding electron excitations for the α phase and β phase. Interband transitions and excitons are denoted by IT and EX, respectively.

exhibits a substantial binding energy of approximately $E_B = 0.37$ eV, with $E_B/E_G \sim 1/3$, in accordance with the scaling universality for monolayer 2D semiconductors [46].

HREELS spectra show four peaks in the β phase, suggesting noticeable splitting in both of the interband transition and exciton peaks [Fig. 3(d)] with the discussion detailed in the SM [41]. These splittings arise from the bonding-antibonding splitting in the LHB and UHB in the β phase. As shown in Fig. 3(f), the splitting of the UHB generates two corresponding excitonic bands. Subsequently, hopping from the LHB antibonding band to the unoccupied bands will generate four different possible excitations: IT1 and IT2, corresponding to transitions to the UHB bonding and antibonding bands, and EX1 and EX2, corresponding to excitations to the two excitonic bands [Fig. 3(f)].

Dimensionality-modulated exciton dispersion—To better visualize the dispersion of the observed excitations, we initially normalized the HREELS mapping for both the α phase [Fig. 4(a)] and the β phase [Fig. 4(b)] by integrating the intensity over the $0.5 - 1.5$ eV energy range at each momentum q [47]. From the normalized HREELS spectra, it is evident that both the IT and the EX features exhibit clear dispersion within the concerned momentum range.

To quantitatively capture the dispersions, we employed a Voigt function to fit the momentum-dependent EDCs. Additionally, to further enhance the clarity of the dispersion near the BZ center, we applied a second derivative to the normalized 2D mapping spectra, which helps highlight the
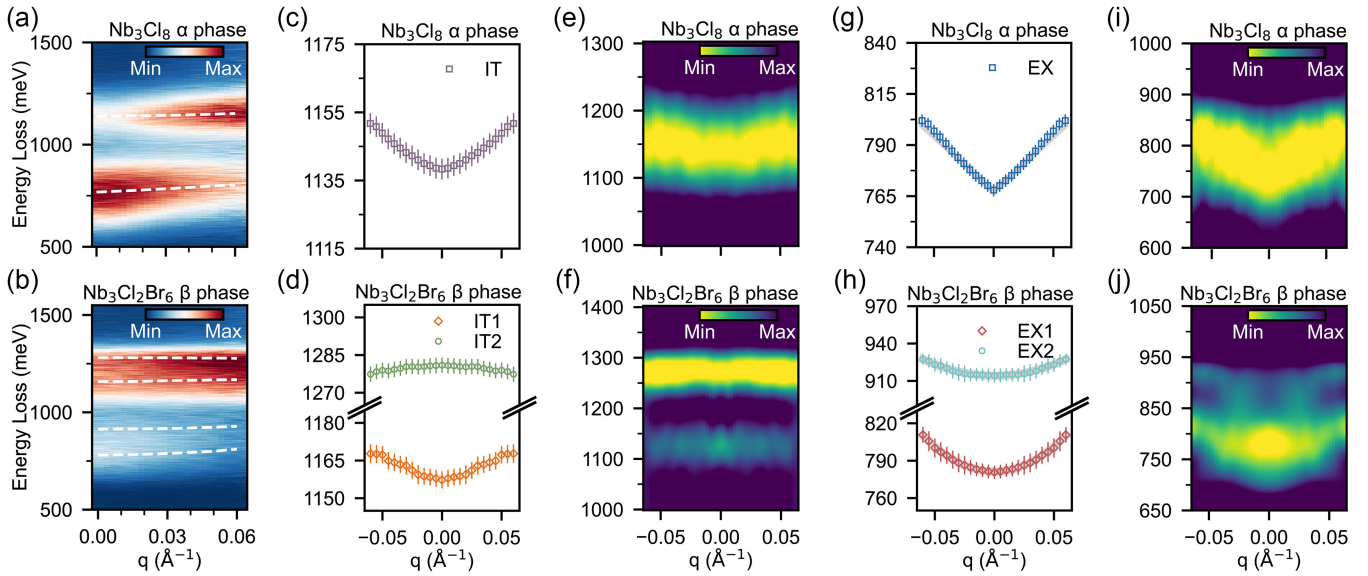
FIG. 4. Exciton dispersions from the HREELS measurements. (a),(b) Normalized HREELS mapping for Nb_3Cl_8 at 300 K (α phase) and $Nb_3Cl_2Br_6$ at 106 K (β phase). The white dashed lines represent the fitting results of the momentum-dependent EDCs. (c), (d) Extracted dispersions of the inter-band transitions for the α phase and β phase, obtained by fitting the experimental data. (e),(f) The second derivative images of the interband transitions for the α phase and β phase. (g),(h) Extracted dispersions of the excitons for the α phase and β phase, with the gray curves represent the linear fit and parabolic fit to the correspond dispersions, respectively. (i),(j) The second derivative images of the exciton dispersions for the α phase and β phase. Notice, to clearly display the dispersion shape near the BZ center, the data in (c)–(j) are symmetrized along the gamma point to show the negative momentum. The error bars are determined through the convolution of instrumental resolution (~3.0 meV) and the standard errors derived from the fitting process (~0.3 meV for the α phase and ~5.0 meV for the β phase).

dispersion shape. The fitted dispersion and the second derivative mapping in both the α phase and β phase show consistent results. First, we investigated the dispersions of the interband transitions in both the α phase [Figs. 4(c) and 4(e)] and β phase [Figs. 4(d) and 4(f)]. Within the concerned momentum range ($|\mathbf{q}| \sim 0.06$ Å^{-1}), the interband transitions both display paraboliclike dispersions near the BZ center, with a flat energy distribution less than 20 meV. Since interband transitions result from the collective contributions of bands throughout the entire BZ, these flat dispersions further consolidate the flatness of the LHB and UHB in both the α and β phases.

Next, we focus on the exciton dispersions. In the β phase, the two excitonic bands, EX1 and EX2, both exhibit clear parabolic dispersion, as evidenced by both the fitted results [Fig. 4(h)] and the second derivative results [Fig. 4(j)]. These results undoubtedly reproduce the expected dispersions of 3D Wannier excitons, consistent with the 3D nature of the β phase. In contrast, in the α phase, the exciton displays a distinctive "V"-shaped dispersion near the $\bar{\Gamma}$ point [Figs. 4(g) and 4(i)], indicating that it is a 2D massless exciton. Within the small momentum range ($|\mathbf{q}| \sim 0.025$ Å^{-1}), the exciton exhibits a clear linear dispersion, which gradually deviates from linearity as $|\mathbf{q}|$ increases. A linear fit of the dispersion near the BZ center ($|\mathbf{q}| \sim 0.025$ Å^{-1}) is given by: $E = E_0 + v \cdot |\mathbf{q}|$, where the

slope $v = 0.51$ eV/Å represents the exciton group velocity, directly reflecting the exciton diffusion speed [16,17].

To fully understand the massless exciton dispersion in the α phase and capture the dramatic changes in dispersion across the phase transition, we employ a modeled Hamiltonian that accounts for the quantum effects of exchange scattering between electron-hole pairs [16,20,50]. In this framework, the exciton dispersion is obtained by solving the Bethe Salpeter equation in the electron-hole basis [42,43,45]. The solution to the Hamiltonian results from the combined effect of the electron-hole transition energy (E_k), the direct interaction (E_d), and the exchange interaction (E_{ex}). Here, E_k contributes to the exciton kinetic energy, while E_d and E_{ex} contribute to the exciton potential energy. Using $\mathbf{q} \cdot \mathbf{p}$ perturbation theory with the modeled Hamiltonian, the contributions of these three interactions in the long-wavelength limit ($|\mathbf{q}| \to 0$) can be expressed as

$$E_k(\mathbf{q}) \propto |\mathbf{q}|^2, \tag{1}$$

$$E_d(\mathbf{q}) \propto -|\mathbf{q}|^2, \tag{2}$$

$$E_{ex}(\mathbf{q}) \propto \begin{cases} \cos^2(\theta_q) + \chi|\mathbf{q}|^2, & \text{(in 3D)} \\ |\mathbf{q}| \cdot \cos^2(\theta_q) + \kappa|\mathbf{q}|^2, & \text{(in 2D)} \end{cases} \tag{3}$$

where θ_q is the angle between the momentum $\boldsymbol{q}$ and the dipole matrix element $\boldsymbol{P}_S$ of the exciton state $|S(\boldsymbol{q})\rangle$, and the factors χ, κ are constants related to the specific band structure of the system. The exciton dispersion near the $\bar{\Gamma}$ point is determined by the competition between these three terms. In 3D systems, the exciton dispersion always manifests a characteristic parabolic shape. In contrast, for 2D systems, the presence of the linear term in E_{ex} induces a distinct linear exciton dispersion near the BZ center, as illustrated in Fig. 1(d). When the parabolic contributions arising from E_k and E_d are dominated by a strong E_{ex} term, the linear behavior of the exciton dispersion persists over an extended range from the BZ center. This enhanced linear regime becomes more accessible for experimental observation through HREELS.

Nb_3Cl_8 is a Mott insulator with relatively flat LHB and UHB. As a result, the kinetic term E_k can be treated as a constant, independent of the momentum $\boldsymbol{q}$, which is consistent with the observed flat dispersion of the IT [Figs. 4(c)–4(f)]. The breathing Kagome lattice structure, which promotes significant overlap of the electron-hole wave functions, further suppresses the Coulomb screening [51,52]. Consequently, Nb_3Cl_8 exhibits enhanced exchange interactions, i.e., E_{ex} dominates the exciton dynamics, providing the primary mechanism behind the observed dimensional dependence of the exciton dispersions. The spontaneous structural phase transition, which notably alters the interlayer coupling strength, establishes Nb_3Cl_8 as an ideal natural platform for investigating excitonic dimensional effects. In the α phase, the strong vdW nature of Nb_3Cl_8 results in negligible interlayer coupling, and thus excitons are confined within the 2D layers, with the in-plane screening effect [53–55] predominantly contributing to the 2D massless linear exciton dispersion. In contrast, in the β phase, the strong interlayer hybridization alters the electronic properties, causing the excitons to no longer be localized within 2D layers. This leads to a more pronounced out-of-plane screening effect, resulting in exciton dispersion that exhibits 3D characteristics.

In summary, we observed exciton splitting across the phase transition of Nb_3Cl_8, originating from bonding-antibonding splitting due to enhanced interlayer coupling. More importantly, in the α phase, we definitively demonstrate the presence of a quasi-2D massless exciton dispersion, which transitions to a 3D parabolic dispersion due to the significant enhancement of interlayer coupling across the phase transition. This unique variation in interlayer coupling strength makes Nb_3Cl_8 an ideal platform for studying the dimensional effects on excitonic band structures. Beyond the qualitative similarities to 2D semiconductors, the correlated nature of Nb_3Cl_8 necessitates advanced many-body treatments. We expect these results to catalyze future theoretical and experimental efforts to clarify the unique excitonic mechanisms in the correlated regime.

Data availability—The data that support the findings of this article are openly available [58].

[1] J. Frenkel, Phys. Rev. **37**, 17 (1931).

[2] H. Haug and S. W. Koch, *Quantum Theory of the Optical and Electronic Properties of Semiconductors* (World Scientific, Singapore, 2009).

[3] G. H. Wannier, Phys. Rev. **52**, 191 (1937).

[4] G. Wang, A. Chernikov, M. M. Glazov, T. F. Heinz, X. Marie, T. Amand, and B. Urbaszek, Rev. Mod. Phys. **90**, 021001 (2018).

[5] J. Madéo, M. K. L. Man, C. Sahoo, M. Campbell, V. Pareek, E. L. Wong, A. Al-Mahboob, N. S. Chan, A. Karmakar, B. M. K. Mariserla, X. Li, T. F. Heinz, T. Cao, and K. M. Dani, Science **370**, 1199 (2020).

[6] M. Reutzel, G. S. M. Jansen, and S. Mathias, Adv. Phys. X **9**, 2378722 (2024).

[7] Z. Ye, T. Cao, K. O'brien, H. Zhu, X. Yin, Y. Wang, S. G. Louie, and X. Zhang, Nature (London) **513**, 214 (2014).

[8] Y. Zhou, G. Scuri, D. S. Wild, A. A. High, A. Dibos, L. A. Jauregui, C. Shu, K. De Greve, K. Pistunova, A. Y. Joe, T. Taniguchi, K. Watanabe, P. Kim, M. D. Lukin, and H. Park, Nat. Nanotechnol. **12**, 856 (2017).

[9] M. Gatti and F. Sottile, Phys. Rev. B **88**, 155113 (2013).

[10] R. Wallauer, R. Perea-Causin, L. Münster, S. Zajusch, S. Brem, J. Güdde, K. Tanimura, K.-Q. Lin, R. Huber, E. Malic, and U. Höfer, Nano Lett. **21**, 5867 (2021).

[11] V. Perebeinos, J. Tersoff, and P. Avouris, Nano Lett. **5**, 2495 (2005).

[12] M. O. Sauer, C. E. M. Nielsen, L. Merring-Mikkelsen, and T. G. Pedersen, Phys. Rev. B **103**, 205404 (2021).

[13] M. Selig, G. Berghäuser, M. Richter, R. Bratschitsch, A. Knorr, and E. Malic, 2D Mater. **5**, 035017 (2018).

[14] C. D. Spataru, S. Ismail-Beigi, R. B. Capaz, and S. G. Louie, Phys. Rev. Lett. **95**, 247402 (2005).

[15] E. Malic, M. Selig, M. Feierabend, S. Brem, D. Christiansen, F. Wendler, A. Knorr, and G. Berghäuser, Phys. Rev. Mater. **2**, 014002 (2018).

[16] D. Y. Qiu, G. Cohen, D. Novichkova, and S. Refaely-Abramson, Nano Lett. **21**, 7644 (2021).

[17] J. J. P. Thompson, S. Brem, M. Verjans, R. Schmidt, S. Michaelis de Vasconcellos, R. Bratschitsch, and E. Malic, 2D Mater. **9**, 025008 (2022).

[18] F. Wu, F. Qu, and A. H. MacDonald, Phys. Rev. B **91**, 075310 (2015).

[19] P. Cudazzo, L. Sponza, C. Giorgetti, L. Reining, F. Sottile, and M. Gatti, Phys. Rev. Lett. **116**, 066803 (2016).

[20] D. Y. Qiu, T. Cao, and S. G. Louie, Phys. Rev. Lett. **115**, 176801 (2015).

[21] H. Yu, G.-B. Liu, P. Gong, X. Xu, and W. Yao, Nat. Commun. **5,** 3876 (2014).

[22] W. Chen, C.-J. Huang, and Q. Zhu, Phys. Rev. Lett. **131,** 236004 (2023).

[23] K. F. Mak, C. Lee, J. Hone, J. Shan, and T. F. Heinz, Phys. Rev. Lett. **105,** 136805 (2010).

[24] A. Splendiani, L. Sun, Y. Zhang, T. Li, J. Kim, C.-Y. Chim, G. Galli, and F. Wang, Nano Lett. **10,** 1271 (2010).

[25] C. Habenicht, M. Knupfer, and B. Büchner, Phys. Rev. B **91,** 245203 (2015).

[26] R. Schuster, J. Trinckauf, C. Habenicht, M. Knupfer, and B. Büchner, Phys. Rev. Lett. **115,** 026404 (2015).

[27] R. Schuster, Y. Wan, M. Knupfer, and B. Büchner, Phys. Rev. B **94,** 085201 (2016).

[28] K. B. Simbulan, T.-D. Huang, G.-H. Peng, F. Li, O. J. Gomez Sanchez, J.-D. Lin, C.-I. Lu, C.-S. Yang, J. Qi, S.-J. Cheng, T.-H. Lu, and Y.-W. Lan, ACS Nano **15,** 3481 (2021).

[29] J. Hong, R. Senga, T. Pichler, and K. Suenaga, Phys. Rev. Lett. **124,** 087401 (2020).

[30] Y.-C. Shih, F. A. Nilsson, and G.-Y. Guo, Phys. Rev. B **110,** 205417 (2024).

[31] X. Zhu, Y. Cao, S. Zhang, X. Jia, Q. Guo, F. Yang, L. Zhu, J. Zhang, E. W. Plummer, and J. Guo, Rev. Sci. Instrum. **86,** 083902 (2015).

[32] S. Grytsiuk, M. I. Katsnelson, E. G. C. P. v. Loon, and M. Rösner, npj Quantum Mater. **9,** 8 (2024).

[33] J. Hu, X. Zhang, C. Hu, J. Sun, X. Wang, H.-Q. Lin, and G. Li, Commun. Phys. **6,** 172 (2023).

[34] Y. Zhang, Y. Gu, H. Weng, K. Jiang, and J. Hu, Phys. Rev. B **107,** 035126 (2023).

[35] S. Gao et al., Phys. Rev. X **13,** 041049 (2023).

[36] Y. Haraguchi, C. Michioka, M. Ishikawa, Y. Nakano, H. Yamochi, H. Ueda, and K. Yoshimura, Inorg. Chem. **56,** 3483 (2017).

[37] J. P. Sheckelton, K. W. Plumb, B. A. Trump, C. L. Broholm, and T. M. McQueen, Inorg. Chem. Front. **4,** 481 (2017).

[38] S. N. Magonov, P. Zoennchen, H. Rotter, H. J. Cantow, G. Thiele, J. Ren, and M. H. Whangbo, J. Am. Chem. Soc. **115,** 2495 (1993).

[39] Z. Sun, H. Zhou, C. Wang, S. Kumar, D. Geng, S. Yue, X. Han, Y. Haraguchi, K. Shimada, P. Cheng, L. Chen, Y. Shi, K. Wu, S. Meng, and B. Feng, Nano Lett. **22,** 4596 (2022).

[40] C. M. Pasco, I. El Baggari, E. Bianco, L. F. Kourkoutis, and T. M. McQueen, ACS Nano **13,** 9457 (2019).

[41] See Supplemental Material at http://link.aps.org/supplemental/10.1103/1z8v-hvkf for details about sample preparation, experimental methods, modeled Hamiltonian, identification of the observed electronic excitations, and HREELS spectra of $Nb_3Cl_2Br_6$ α phase, including Figs. S1–S4 and Refs. [16,20,35,39,40,42–45].

[42] G. Strinati, La Rivista del Nuovo Cimento (1978-1999) **11,** 1 (1988).

[43] M. Rohlfing and S. G. Louie, Phys. Rev. B **62,** 4927 (2000).

[44] J. Li, Z. Lin, G. Miao, W. Zhong, S. Xue, Y. Li, Z. Tao, W. Wang, J. Guo, and X. Zhu, Surf. Sci. **721,** 122067 (2022).

[45] J. Deslippe, G. Samsonidze, D. A. Strubbe, M. Jain, M. L. Cohen, and S. G. Louie, Comput. Phys. Commun. **183,** 1269 (2012).

[46] Z. Jiang, Z. Liu, Y. Li, and W. Duan, Phys. Rev. Lett. **118,** 266401 (2017).

[47] In HREELS measurements, incident electrons interact with the long-range dipole field generated by electronic excitations within the material [48,49]. As a result, the loss signals are confined to the dipole scattering region, leading to a rapid attenuation of signal intensity as the scattering angle deviates from specular scattering. Consequently, this limits visualization of electronic excitation dispersion in raw HREELS spectra.

[48] H. Ibach, Electron Energy Loss Spectrometers: The Technology of High Performance (Springer-Verlag, Berlin, 1991).

[49] E. Evans and D. L. Mills, Phys. Rev. B **5,** 4126 (1972).

[50] L. C. Andreani and F. Bassani, Phys. Rev. B **41,** 7536 (1990).

[51] H. Ishii, T. Nakayama, and J.-i. Inoue, Phys. Rev. B **69,** 085325 (2004).

[52] G. Sethi, Y. Zhou, L. Zhu, L. Yang, and F. Liu, Phys. Rev. Lett. **126,** 196403 (2021).

[53] Q. Guo et al., Nature (London) **613,** 53 (2023).

[54] K. Tanaka, F. Sano, T. Takahashi, T. Kondo, R. Ito, and K. Ema, Solid State Commun. **122,** 249 (2002).

[55] K. Tanaka, T. Takahashi, T. Kondo, T. Umebayashi, K. Asai, and K. Ema, Phys. Rev. B **71,** 045312 (2005).

[56] H. Raether, Excitation of Plasmons and Interband Transitions by Electrons, Springer Tracts in Modern Physics (Springer, Berlin, Heidelberg, 2006).

[57] S. Vig, A. Kogar, M. Mitrano, A. A. Husain, V. Mishra, M. S. Rak, L. Venema, P. D. Johnson, G. D. Gu, E. Fradkin, M. R. Norman, and P. Abbamonte, SciPost Phys. **3,** 026 (2017).

[58] Z. Su et al., 2026, 10.6084/m9.figshare.31324483.

End Matter

Principle of the 2D HREELS—HREELS probes elementary excitations via the inelastic scattering of a monochromatic electron beam [56]. In traditional HREELS measurements, which employ a fixed scattering geometry (with fixed incident and scattering angles), an EDC is acquired at a single momentum point. By analyzing the energy and angle of the monochromatic electron beam before and after scattering, the energy of the elementary excitation and the momentum parallel to the sample surface can be determined based on the principles of energy and momentum conservation [Fig. 5(a)] [48]:

$$E_{Loss} = E_i - E_s, \tag{A1}$$

$$q_\parallel = \frac{\sqrt{2mE_i}}{\hbar}\left(\sin\alpha_i - \sqrt{1 - \frac{E_{Loss}}{E_i}}\sin\alpha_s\right), \tag{A2}$$
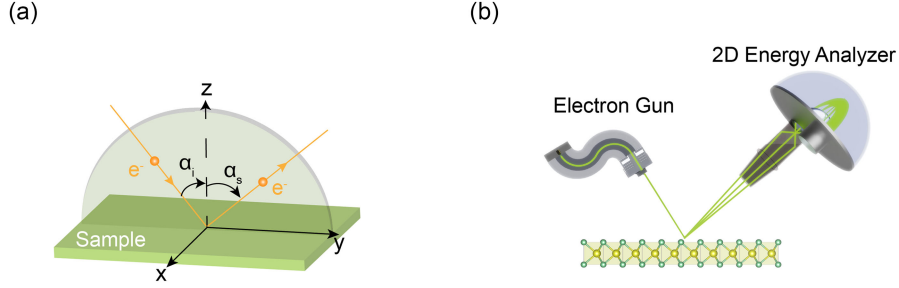
FIG. 5. (a) Schematic of the scattering geometry. (b) Schematic of the experimental setup of the 2D HREELS.

where E_i and E_s are the energy of incident and scattering electrons, in sequence. To acquire the dispersion of elementary excitations, it is necessary to change the momentum points by rotating the angles of the analyzer, sample, and monochromator.

In contrast, our HREELS setup is equipped with a hemispherical energy analyzer, enabling 2D mapping of momentum and energy simultaneously without the need to rotate the sample or analyzer, significantly enhancing data acquisition efficiency [Fig. 5(b)]. Under this instrumental configuration, the ultimate energy and momentum resolutions can reach 0.7 meV and 0.002 Å^{-1}, respectively [31]. In the present Letter, to optimize detection efficiency and ensure a high signal-to-noise ratio for the observed excitonic features, we utilized an operating energy resolution of 3.0 meV and a momentum resolution of 0.005 Å^{-1}. *In situ* HREELS measurements in this Letter were performed using a monochromatic electron beam with an incident angle of 60- and an incident energy of 110 eV.

Probing depth of HREELS—While HREELS is typically characterized as a surface-sensitive technique, the effective probing depth depends fundamentally on the underlying scattering mechanism. It is essential to distinguish between impact scattering and dipole scattering. In the impact scattering regime, the probing depth is governed by the inelastic mean free path of the probe electrons—typically $5 - 10$ Å for incident energies in the $50 - 100$ eV range—rendering the technique strictly sensitive to the topmost atomic layers.

In contrast, the dipole scattering mechanism, which dominates the excitonic measurements near the Γ point in this Letter, involves long-range electromagnetic interactions. In this regime, the probing depth is independent of the inelastic mean free path. The HREELS cross section is directly proportional to the spectral function $S(\boldsymbol{q}, \omega)$, which describes the collective electronic response of the system [57]:

$$S(\boldsymbol{q}, \omega) = \int_{-\infty}^{0} S(\boldsymbol{q}, z, z', \omega) e^{-|\boldsymbol{q}| \cdot |z+z'|} dz dz',$$

where z and z' are coordinates perpendicular to the surface. The term $S(\boldsymbol{q}, z, z', \omega)$ represents the density-density correlation function:

$$S(\boldsymbol{q}, z, z', \omega) = \sum_{m,n} \left[\langle m | \hat{\rho}(\boldsymbol{q}, z) | n \rangle \cdot \langle n | \hat{\rho}(-\boldsymbol{q}, z') | m \rangle P_m \right]$$
$$\cdot \delta(E - E_n + E_m),$$

where $\hat{\rho}$ is the charge density operator, $P_m = e^{-E_m/k_B T}/Z$ is the Boltzmann factor, and $|m\rangle$, $|n\rangle$ denote the many-body states of the sample with energies E_m and E_n, respectively.

Crucially, the weighting factor $e^{-|\boldsymbol{q}| \cdot |z+z'|}$ in the integral dictates that the effective probing depth scales as $\sim 1/|\boldsymbol{q}|$. Within our investigated momentum range (0.00 to 0.06 Å^{-1}), the probing depth extends significantly beneath the surface, thereby encompassing multiple van der Waals layers. Consequently, the excitonic signals detected in Nb_3Cl_8 originate from the collective response of many near-surface layers, effectively representing the intrinsic bulk-like properties of the material. This ensures that the observed evolution of exciton dispersion is a manifestation of dimensionality-driven effects rather than a localized surface phenomenon.